



1 **Understanding the resilient carbon cycle response to the 2014–2015**
2 **Blob event in the Gulf of Alaska using a regional ocean biogeochemical**
3 **model**

4 Yumi Abe¹, Takamitsu Ito¹, Amanda H. V. Timmerman², Christopher T. Reinhard¹, Joseph P. Montoya³

5 ¹School of Earth and Atmospheric Sciences, Georgia Institute of Technology, Atlanta, 30332-0340, U.S.A.

6 ²Virginia Institute of Marine Science, Gloucester Point, 23062-1346, U.S.A.

7 ³School of Biological Sciences, Georgia Institute of Technology, Atlanta, 30332-0230, U.S.A.

8

9 *Correspondence to:* Yumi Abe (yumiabe@gatech.edu)

10 **Abstract.** Marine heatwaves (MHWs), characterized by anomalously high sea surface temperatures, are occurring with
11 increasing frequency and intensity, profoundly impacting ocean circulation, biogeochemistry, and marine ecosystems. The
12 MHW known as the Blob, which persisted in the subarctic NE Pacific from 2014 to 2015, significantly affected surrounding
13 ecosystems. Warming-induced solubility reduction is expected to raise the partial pressure of carbon dioxide (pCO₂) in the
14 surface water, causing outgassing of CO₂ to the atmosphere. Outgassing of CO₂ is another source of atmospheric CO₂ in
15 addition to anthropogenic fossil fuel burning. However, moored observations at Ocean Station Papa (OSP; 145°W, 50°N)
16 shows a moderate decrease in oceanic pCO₂ during the Blob, resisting the warming-induced outgassing of CO₂. This response
17 is opposite of what is expected from warming alone, and instead has been attributed to reductions in dissolved inorganic carbon
18 (DIC), although the mechanisms driving this reduction have remained unclear. We employed a regional model that accurately
19 reproduces the temporal variability of oceanic pCO₂ at OSP to investigate the cause of decrease pCO₂ during the Blob. The
20 analysis of model outputs indicates that the observed oceanic pCO₂ decline resulted from the offset between warming-induced
21 solubility reduction (increasing pCO₂) and weakened physical transport of DIC (decreasing pCO₂), with the latter dominating.
22 Both horizontal and vertical transports played important roles. The near-surface carbon budget over the broad region was
23 primarily driven by changes in the vertical transport. The decrease in DIC during the Blob resulted from the suppression of
24 upwelling of DIC-rich subsurface waters in the winter of 2013. In this period, the horizontal transport also contributed
25 substantially to DIC reduction. In particular, at OSP, the effect of the horizontal transport was comparable to that of the vertical
26 transport, reflecting the northward advection of low-DIC water masses. These findings indicate that changes in physical
27 circulation were the primary driver of the moderately enhanced CO₂ uptake observed during the Blob. This study provides a
28 critical insight into the complexity of biogeochemical response to extreme warming events and underscores the importance of
29 resolving physical transport processes in assessing oceanic carbon uptake during MHWs.



30 **1 Introduction**

31 Approximately 25% of historical anthropogenic carbon emission has been absorbed by the oceans (Friedlingstein et al., 2022),
32 and the North Pacific is one of the major regions for ocean carbon uptake (Takahashi et al., 2009). The carbon exchange
33 between the atmosphere and ocean is closely related to ocean temperature through its influences on the solubility of carbon
34 dioxide (CO₂) in seawater. In recent years, anomalously high ocean temperatures are frequently observed, known as marine
35 heatwaves (MHWs; Hobday et al., 2016). With the ongoing progression of global warming, the frequency and intensity of
36 MHWs have been increasing (Frölicher et al., 2018; Oliver et al., 2018). In particular, the persistent MHW that occurred in the
37 subarctic NE Pacific from the winter of 2013 to 2015, known as *the Blob* (Bond et al., 2015), had severe impacts on surrounding
38 ecosystems (Cavole et al., 2016; Smale et al., 2019) and fisheries (Barbeaux et al., 2020). This anomalously high ocean
39 temperature was attributed to weaker surface winds, which reduced ocean surface heat loss, and weakened horizontal and
40 vertical mixing (Bond et al., 2015; Di Lorenzo and Mantua, 2016).

41

42 Biogeochemical variables are also impacted by MHWs. In particular, low-oxygen and acidification become more pronounced
43 during MHWs (Gruber et al., 2021; Burger et al., 2022; Li et al., 2024b). These changes are driven by alterations in ocean
44 circulation driven by winds and air-sea interactions associated with atmospheric anomalies that induce the MHWs, and also
45 by the direct effects of high temperatures, including enhanced stratification, reduced solubility, and changes in biological
46 activity. During the Blob, both surface dissolved oxygen and inorganic carbon (DIC) were significantly decreased due to
47 reduced solubility caused by rising water temperatures (Mogen et al., 2022).

48

49 For the air-sea CO₂ exchange, the uptake in the North Pacific decreases by 29±11% during persistent MHWs mainly due to
50 the direct effect of increase in water temperature (Mignot et al., 2022). However, this reduction in ocean carbon uptake is
51 primarily driven by the substantial increase in oceanic CO₂ outgassing in the tropical Pacific. Focusing on the subarctic regions,
52 the oceanic CO₂ uptake increases during the MHWs. For example, mooring data from Ocean Station Papa (OSP; 50°N, 145°W)
53 in the eastern North Pacific, which is one of the longest-running observation sites, indicate the low surface DIC and oceanic
54 partial pressure of CO₂ (pCO₂) during a more recent MHW (Kohlman et al., 2024). In the Gulf of Alaska (GOA), air-sea CO₂
55 flux exhibited a negative anomaly (stronger ocean uptake) of approximately 45% relative to the climatological monthly means
56 during the Blob based on a machine-learning based reconstruction (Duke et al., 2023). The enhanced ocean carbon uptake is
57 caused by the decrease in oceanic pCO₂ in the subarctic North Pacific, which is driven by the effects of reduced surface ocean
58 DIC. However, the processes responsible for this DIC reduction is not fully understood (Mignot et al., 2022; Li et al., 2024a).
59 Furthermore, estimates of oceanic pCO₂ changes derived from observation-based products are subject to considerable
60 uncertainty, as observational data in the subarctic North Pacific are temporally and spatially sparse. Consequently,
61 discrepancies among data products restrict the robustness of their assessments (Li et al., 2024a).

62



63 To elucidate the mechanisms by which the MHWs lead to the observed changes in oceanic pCO₂ and air-sea CO₂ fluxes,
64 numerical models can provide the carbon mass balance and exploring underlying physical and biogeochemical processes.
65 Physical processes that control the regional ocean circulation, biogeochemical cycling, and air-sea gas exchanges often occur
66 at scales smaller than several tens of kilometres, which remain unresolved in global earth system models (Gruber et al., 2021).
67 In the subarctic NE Pacific, reproducing the full variability of oceanic pCO₂ in models is complicated by boundary currents
68 and eddies that transport macro- and micro-nutrients, alkalinity and DIC. A previous study using a coarse resolution model
69 (McKinley et al., 2006) has shown that although models captured the variability of individual components of oceanic pCO₂ on
70 seasonal and interannual timescales, they have not fully reproduced the total variability of oceanic pCO₂, and their ability to
71 simulate the temporal patterns of air-sea CO₂ fluxes remains limited.

72

73 There are several regional modeling studies exploring biogeochemical processes in the GOA. Coyle et al. (2012) developed
74 regional, biogeochemical simulations for the northern GOA based on the ROMS circulation model with the horizontal
75 resolution of 3 km from 2001 to 2004 focusing on the coastal regions. The biogeochemical model component is based on the
76 GOANPZ model (Hinckley et al., 2009). The model reproduced the spring phytoplankton bloom from the continental shelves
77 to the open ocean. This model subsequently was used to analyze ocean acidification with the inclusion of carbonate chemistry
78 (Siedlecki et al., 2017). Hauri et al. (2020) developed a hindcast simulation for the similar northern GOA domain. They also
79 used the ROMS physical model with 4.5 km horizontal resolution. The biogeochemical component is based on the COBALT
80 biogeochemistry model (Stock et al., 2014) with specific modifications to capture coastal ecosystems. Following these previous
81 studies, we constructed a regional biogeochemical and carbon cycle model for the GOA. The model has been validated against
82 a suite of physical and biogeochemical observations (Ito et al., 2025). This study expands the model to include a validated
83 carbon cycle component. The simulated temporal variability of oceanic pCO₂ is validated with the NOAA (Pacific Marine
84 Environmental Laboratory's Ocean Climate Stations and Carbon groups) mooring at OSP (Emerson et al., 2011; Cronin et al.,
85 2015). The model outputs are used to understand the underlying mechanisms and to quantify the changes in oceanic pCO₂ in
86 this critical carbon sink during the Blob. This paper includes the description of the model and the observational data used for
87 model validation (section 2), and the results of oceanic pCO₂ variations during the Blob and its causes (section 3). Conclusions
88 and discussion (section 4) summarizes this study with the potential impacts of high ocean temperature anomalies on regional
89 carbon cycle, their effects on the wider ocean basin, and possible future implications (section 4).

90 **2 Data and Methods**

91 **2.1 Model description**

92 The regional ocean circulation and biogeochemistry model used in this study follows the configuration described in Ito et al.
93 (2025), thus only a brief description is provided here, while full details can be found in their paper. The model is based on
94 MITgcm (Marshall et al., 1997a, b) combined with an ocean biogeochemical model, Biogeochemistry with Light, Iron,



95 Nutrients and Gases (BLING) version 2 (Dunne et al., 2020) including 10 tracers, DIC, alkalinity, O₂, PO₄, NO₃, dissolved Fe,
96 silica, dissolved organic P, and dissolved organic N. The model is driven by 3-hourly averaged atmospheric variables from the
97 JRA-55-do reanalysis data (Tsujino et al., 2018), including the surface air temperature, humidity, 10 m wind stress,
98 precipitation (both rain and snow), river runoff, and downward shortwave and longwave radiation. The earlier simulations of
99 Ito et al. (2025) included a positive bias in sea surface salinity (SSS) of approximately +0.2 psu. To maintain SSSs close to the
100 observations, we applied Newtonian relaxation to SSS toward monthly climatology from World Ocean Atlas 2023 (Reagan et
101 al., 2024) with a restoring timescale of 30 days in the surface grid box of 10 m thickness. The model has a horizontal resolution
102 of 10 km with 42 vertical layers on a latitude-longitude z-level grid. The bathymetry was generated by interpolating the
103 ETOPO2 global 2-minute resolution topography dataset. The model domain has a southern open boundary at 42°N and a
104 western open boundary at 160°W. Vertical mixing was parameterized using the K-profile Parameterization (KPP) scheme
105 (Large et al., 1994) as implemented in MITgcm. The default configuration, including the non-local convection term, was used
106 for this study. KPP diffusivities were applied to momentum and all tracers. A sea ice model, implemented using the MITgcm
107 sea ice package (Losch et al., 2010) and coupled to the ocean component, was used to represent sea ice dynamics and
108 thermodynamics, as well as their influence on surface heat, freshwater, and momentum fluxes.

109

110 Both the initial and boundary conditions in our model also follow Ito et al. (2025). Open boundary conditions are set to the
111 climatological values from GLODAPv2 (Lauvset et al., 2022) for most of the biogeochemical properties. However, for DIC,
112 the open boundary conditions include time-dependent anthropogenic carbon rather than climatology. Temporal changes in
113 DIC due to anthropogenic influences are imposed according to the rate of change in atmospheric CO₂ fractions measured at
114 the Mauna Loa Observatory (Keeling et al., 2001) and its spatial structure is set to the anthropogenic carbon estimates from
115 the GLODAPv2. The model integration was performed through 2017, and the physical open boundary conditions were taken
116 from the oceanic reanalysis data of Simple Ocean Data Assimilation (SODA) version 3 (Carton and Giese, 2008; Carton et al.,
117 2018).

118

119 Several biogeochemical parameters were adjusted to improve the model representation of the carbon cycle. These
120 modifications primarily involved processes related to strength of photosynthesis and remineralization. The modeled default
121 parameters for photosynthetic rates caused excessively high rates in coastal waters, resulting in unrealistically elevated primary
122 production. To address this, the self-shading effect of phytoplankton is turned on, which regulates the light available for
123 phytoplankton growth in the highly productive coastal waters. The bio-optical parameterization of Manizza et al. (2005) is
124 used in our configuration but the background attenuation coefficient in this bio-optical model was reduced to one-quarter of
125 its default value to re-calibrate the net primary production (NPP). Furthermore, the simulated oceanic pCO₂ is highly sensitive
126 to the production of organic matter and the subsequent remineralization. A key factor is the export ratio which determines the
127 fraction of NPP that sinks as particulate organic matter from the surface layer and is subsequently recycled in the subsurface
128 waters. Among the relevant parameters, the partitioning of particulate organic versus dissolved organic matter exerts a



129 particularly strong influence on the representation of oceanic pCO₂. To better capture observed oceanic pCO₂, we adjusted this
130 parameter so that 30% of NPP is converted to dissolved organic matter, compared with a default value of 10%, which means
131 that more organic matter is recycled in the surface layer than the default configuration.

132 **2.2 Observations**

133 To evaluate the model skills in reproducing the observed oceanic pCO₂, SeaFlux data (Fay et al., 2021) are used for spatial
134 comparisons, and NOAA CO₂ mooring data (Emerson et al., 2011; Cronin et al., 2015) are used for temporal comparisons at
135 OSP. SeaFlux data consists of six global observation-based gridded products that reconstruct spatiotemporally continuous
136 estimates of air-sea CO₂ fluxes using different gap-fill methods on the surface oceanic pCO₂ observations. Because the spatial
137 resolution of SeaFlux is one degree in latitude and longitude, our model output was remapped to the same resolution using
138 nearest-neighbour interpolation for comparison. In June 2007, a surface CO₂ mooring time series was initiated at OSP by S.
139 Emerson for the study of North Pacific Carbon Cycle, and the mooring observation has been continued by NOAA Office of
140 Climate Observations. This data provides both physical and biogeochemical variables. For comparison with the model,
141 temperature, salinity, and both oceanic and atmospheric pCO₂ data were obtained from the mooring dataset archived at
142 https://www.ncei.noaa.gov/access/ocean-carbon-acidification-data-system/oceans/Moorings/Papa_145W_50N.html (last
143 access: 1 Oct 2025). For comparison, OSP in the model was represented by averaging all grid points within a 24 km radius of
144 50°N, 145°W.

145 **2.3 Analysis methods**

146 The oceanic pCO₂ anomalies are decomposed as:

$$148 \quad \delta pCO_2 \approx \frac{\partial pCO_2}{\partial T} \delta T + \frac{\partial pCO_2}{\partial S} \delta S + \frac{\partial pCO_2}{\partial DIC^*} \delta DIC^* + \frac{\partial pCO_2}{\partial ALK^*} \delta ALK^* \quad (1)$$

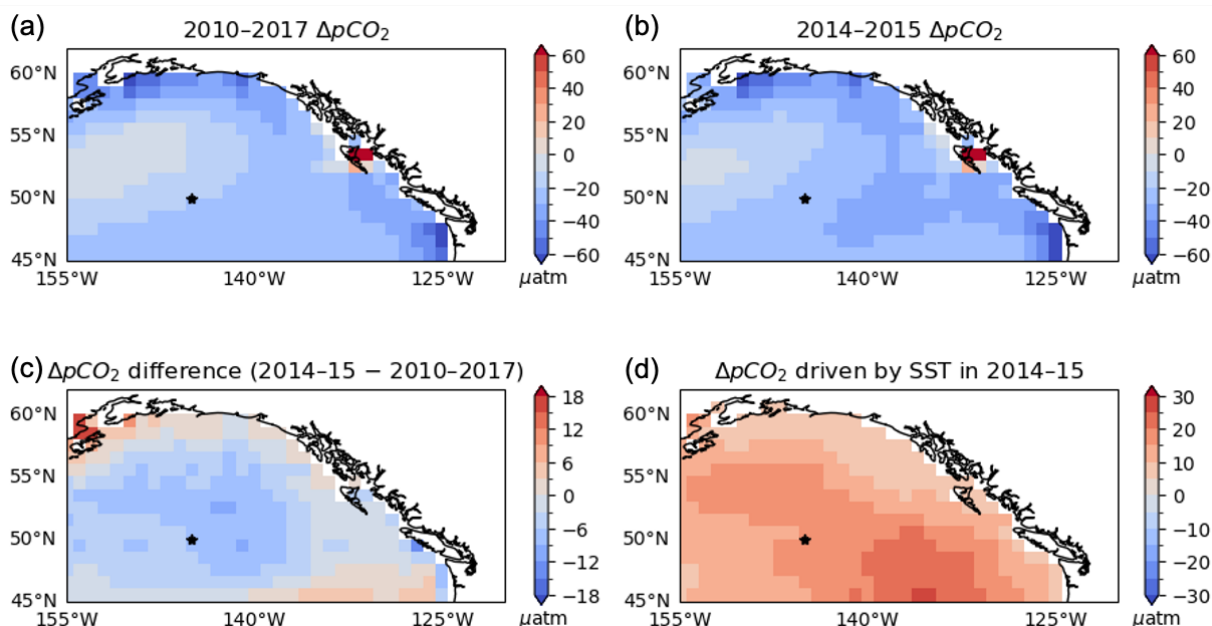
149 where oceanic pCO₂ is a function of sea surface temperature (SST; T), SSS (S), sea surface salinity-normalized DIC (DIC^{*})
150 and sea surface salinity-normalized alkalinity (ALK^{*}). The contributions of these four variables to the oceanic pCO₂ anomalies
151 are calculated using the Python toolbox PyCO2SYS (Humphreys et al., 2022) version 1.8.3. For the input variables, DIC and
152 alkalinity were normalized to a salinity of 35 to eliminate the influence from evaporation and dilution (Keeling et al., 2004).
153 The partial derivatives were evaluated at each time step by perturbing each variable independently while holding the others
154 constant. For this calculation, the constants were set to the median of the temporal variations, and the perturbations were
155 applied with an amplitude equal to the standard deviation. The results were obtained for each grid, and the values at OSP were
156 as follows: $\partial pCO_2 / \partial T = 15.27 \mu atm / ^\circ C$, $\partial pCO_2 / \partial S = 25.26 \mu atm / psu$, $\partial pCO_2 / \partial DIC^* = 2.15 \mu atm / \mu mol kg^{-1}$, $\partial pCO_2 / \partial ALK^* = -1.76 \mu atm / \mu mol kg^{-1}$. In the oceanic pCO₂ decomposition analysis, all input variables were detrended and
157 deseasonalized using the STL function from the statsmodels.tsa.seasonal module in Python.



160 3 Results

161 3.1 Observational evidence of $\Delta p\text{CO}_2$ during marine heatwave

162 Seaflux pCO₂ data reveal the basin-scale surface oceanic pCO₂ climatologies and anomalies during the Blob. Annual mean
163 climatology (2010–2017) shows negative $\Delta p\text{CO}_2$ (oceanic pCO₂ is smaller than the atmospheric pCO₂), indicating that the
164 GOA is on average a sink of atmospheric CO₂ (Fig. 1a). Positive SST anomalies are expected to reduce CO₂ saturation in the
165 ocean and consequently increase oceanic pCO₂. However, observation-based data show a decrease in oceanic pCO₂,
166 accompanied by a larger amplitude of $\Delta p\text{CO}_2$ than non-heatwave conditions during the Blob. This indicates that surface ocean
167 absorbed more CO₂ from the atmosphere during the Blob (2014–2015), and is especially evident in the central GOA (Fig. 1b,
168 c). This trend is at odds against the rising SST, which tends to increase the oceanic pCO₂ and reduce ocean carbon uptake (Fig
169 1d). An estimated contribution of the positive SST anomalies indicates that $\Delta p\text{CO}_2$ should increase across the entire region
170 (Fig. 1d). Therefore, elevated SST cannot account for the observed decrease in $\Delta p\text{CO}_2$ during the Blob.



171
172 **Figure 1: $\Delta p\text{CO}_2$ (oceanic pCO₂ minus atmospheric pCO₂) comparison the Blob and climatology in SeaFlux. Blue shows CO₂ uptake,**

173 and red shows CO₂ outgassing. The star in each panel indicates the location of OSP. Oceanic pCO₂ driven by SST is calculated using

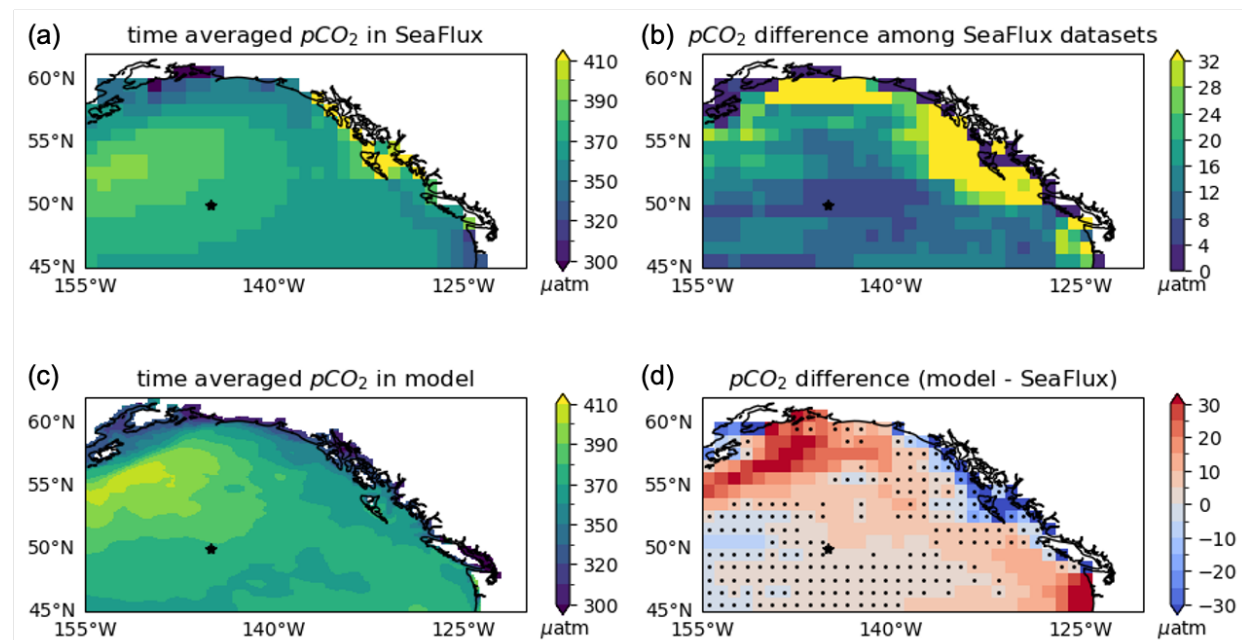
174 SST from SODA version 3.4.2 and DIC and alkalinity from GLODAPv2.

175 3.2 Model validation

176 Before using the model to address the underlying mechanism behind the oceanic pCO₂ decreases during the Blob, the ability
177 of the model to reproduce existing observations must be evaluated. We first examine the model output for the time-averaged
178 oceanic pCO₂ in the GOA from 2010 to 2017. Compared to the ensemble mean of the time-averaged oceanic pCO₂ in the
179 SeaFlux dataset, the spatial correlation is moderately positive ($r=0.30$), and the model generally reproduces the broad

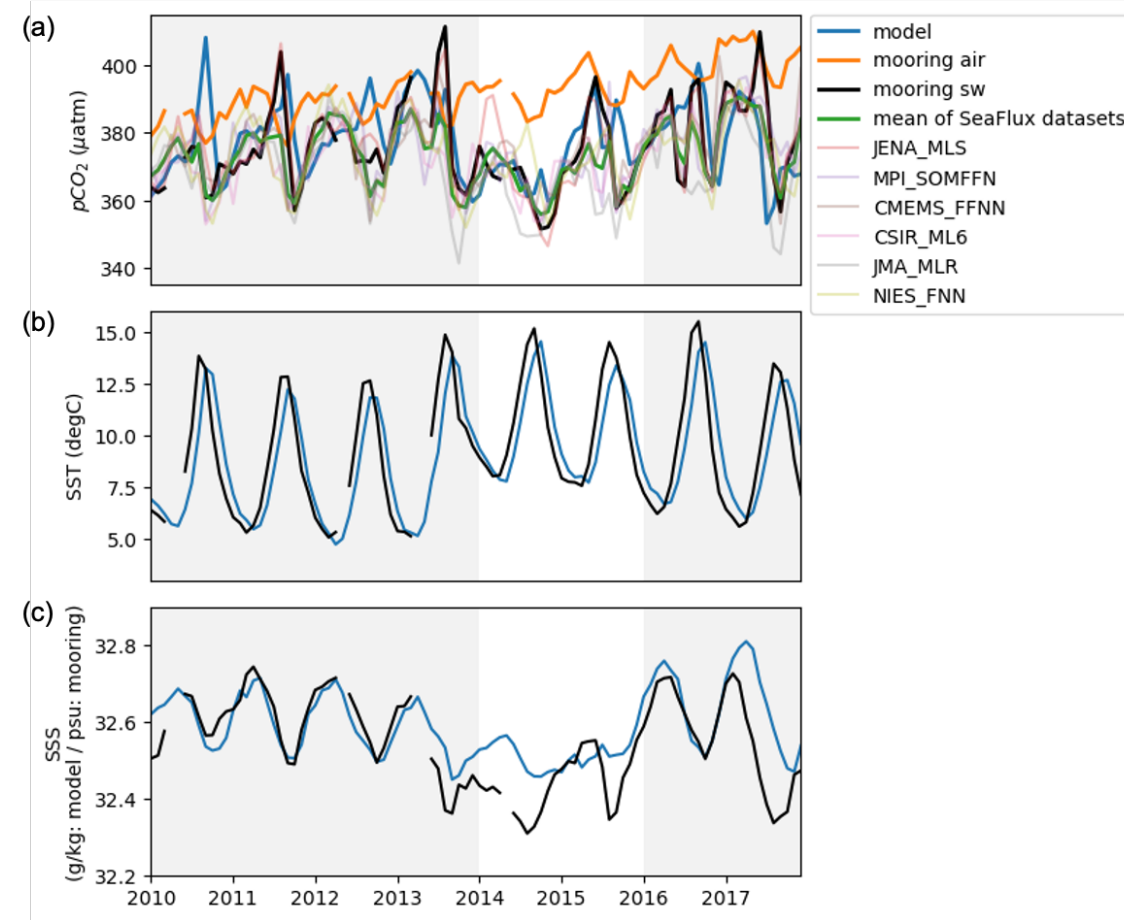


180 climatological spatial distribution of the observed oceanic pCO₂ (Fig. 2a, c). The model overestimated the oceanic pCO₂ in the
181 northwestern area, which likely arises from model circulation biases in this region. Compared to satellite observations, the
182 model has slightly weaker horizontal geostrophic flow, and the core of the subpolar circulation is shifted northward (Ito et al.
183 2025). The modeled vertical stratification is slightly weakened relative to the climatological observations, and this weak
184 stratification bias leads to a higher oceanic pCO₂ in the model. To evaluate the uncertainties in the SeaFlux dataset, variability
185 among the different observational ensembles must be considered. In the open ocean, modeled oceanic pCO₂ is within the range
186 of SeaFlux ensemble variability (Fig. 2b, d). Therefore, in most areas, the model is within the uncertainty bounds of the
187 observation-based oceanic pCO₂.



188
189 **Figure 2: Comparison of oceanic pCO₂ distributions between the model and SeaFlux. The star in each panel indicates the location**
190 **of OSP. Dots in (d) indicate the grid points where the modeled climatology falls within the range of differences among the SeaFlux**
191 **ensemble datasets.**

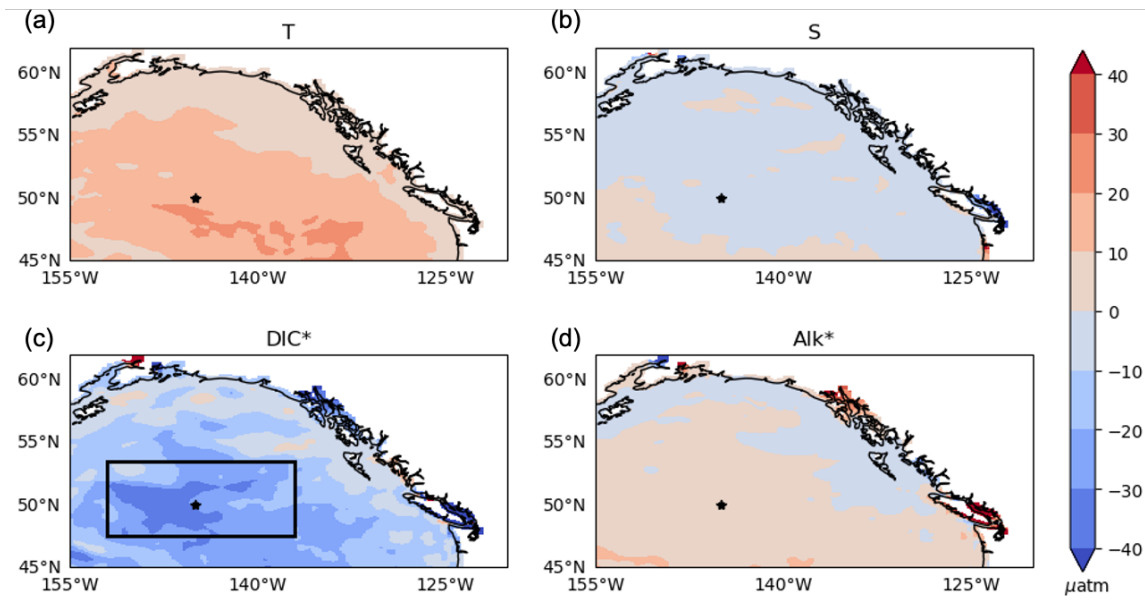
192
193 The model also reproduces the temporal variation in oceanic pCO₂ to a reasonable extent. Compared with the mooring time
194 series at OSP, the model captures the observed variability and magnitude in both biogeochemical and physical variables (Fig.
195 3). For oceanic pCO₂, the model reproduces a statistically significant fraction of the mooring pCO₂ variability ($r=0.44$,
196 normalized-RMSE=1.01), and falls within the spread of the SeaFlux ensemble data. During the Blob, both the mooring
197 observations and model show pronounced decline in oceanic pCO₂. Correspondingly, $\Delta p\text{CO}_2$, which represents the difference
198 between the black or blue line and the orange line in Fig. 3a also decreases. The model slightly overestimated SSS (~0.1 psu)
199 compared to the mooring during the Blob, but this does not significantly compromise the stratification in the model, because
200 the density is primarily governed by sea water temperature in this region.



201
202 **Figure 3: Comparison of time series between the model and mooring observations at OSP for (a) oceanic pCO_2 , (b) SST, and (c) SSS.**
203 In (a), atmospheric pCO_2 from the mooring observations is additionally shown in orange (mooring air) to illustrate variation in
204 ΔpCO_2 . Oceanic pCO_2 from the SeaFlux ensemble mean is also shown in green, with individual ensembles indicated by thin lines
205 with different colors. In (b) and (c), the model is blue and mooring (seawater, sw) is black. The unshaded period corresponds to
206 2014–2015, during which the Blob occurred.

207 3.3 Decomposition of pCO_2 variability

208 Oceanic pCO_2 fluctuations can be explained by four components: temperature, salinity, DIC^* and ALK^* (Eq. 1). The
209 decomposition is applied to the variability of oceanic pCO_2 at OSP, revealing that the warming-induced increase in oceanic
210 pCO_2 is fully compensated by the opposing changes in DIC during the Blob. First, the detrended and deseasonalized oceanic
211 pCO_2 time series is calculated and averaged within the 24 km radius of OSP. Similarly, the time series of the SST, SSS, DIC^* ,
212 and ALK^* are calculated and Eq. (1) is applied to estimate the oceanic pCO_2 anomalies (Fig. 4). The oceanic pCO_2 changes
213 from SSS and ALK^* are small, while SST and DIC^* changes are the main drivers of the oceanic pCO_2 changes. Observations
214 show that oceanic pCO_2 increases due to SST changes during the Blob by about $+20 \mu\text{atm}$, but decreasing oceanic pCO_2 from
215 DIC^* changes is even larger, around $-30 \mu\text{atm}$. Therefore, the net changes in oceanic pCO_2 caused by SST and DIC are



224
 225 **Figure 5: Spatial patterns of the contributions to oceanic pCO₂ from (a) SST, (b) SSS, (c) DIC*, and (d) ALk* during 2014–2015.**
 226 Blue shows CO₂ uptake, and red shows CO₂ outgassing. The star in each panel marks the location of OSP. The black box (47.5–
 227 53.5°N, 208–223°E) in (c) indicates the open-ocean area used for the budget analysis shown in Figs. 6 and 7.

228 The decrease in DIC during the Blob happens not only at OSP but throughout the whole central GOA. Figure 5 shows the
 229 spatial distributions of the oceanic pCO₂ changes calculated from the model outputs of each variable, same as in Fig. 4 during
 230 the Blob. The characteristic described above, namely, the mutual compensation between the SST and DIC, also holds in the
 231 entire region. These two factors counteract each other, resulting in a relatively small decrease in oceanic pCO₂ due to the larger
 232 decrease in DIC. The magnitude of the oceanic pCO₂ decline peaks in the central GOA around the location of OSP.

233 **3.4 Simulated DIC mass balance**

234 To investigate the factors causing the significant decrease in DIC during the Blob, the surface ocean DIC mass balance is
 235 examined by the diagnosis of the DIC tendency terms. In the simplest form, the DIC mass balance is explained by three
 236 components: physical transport, biological activity, and air–sea gas exchanges.

237
$$dC/dt = (\text{transport}) + (\text{biological activity}) + (\text{air} - \text{sea gas transfer}) \quad (2)$$

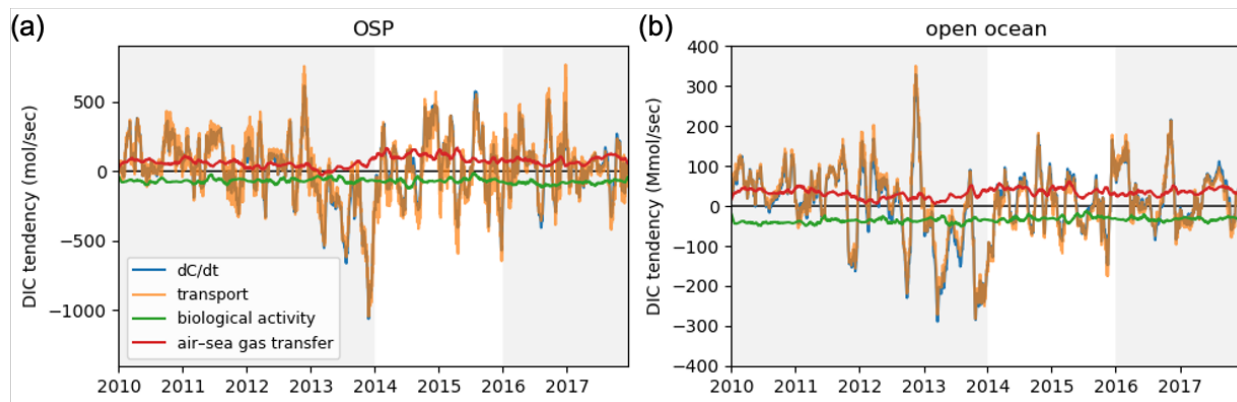
238 On the right-hand side of Eq. 2, the transport term includes resolved advective transport convergence and parameterized mixing
 239 terms. Zonal, meridional and vertical advection of DIC, parameterized mixing, as well as the total transport convergence are
 240 calculated online and recorded as daily means. Biological activity includes the net effects of photosynthetic carbon fixation,
 241 phytoplankton mortality, remineralization of dissolved and particulate organic matter, and the production and dissolution of
 242 calcium carbonates. These carbon tendency terms (dC/dt) are calculated for each timesteps and are recorded as daily averages.



245 The tendency terms calculated at OSP are integrated over the 24-km radius centred at OSP. For the larger open-ocean
 246 surrounding the OSP, they are calculated within 47.5–53.5°N, 208–223°E, indicated by the black box in Fig. 5c. In both cases,
 247 the tendencies are integrated from the surface to 177.5 m, with units of molCs^{-1} . This depth range is greater than the maximum
 248 mixed layer depth diagnosed in our simulation and thus guarantees that vertical integration contains the entire mixed layer
 249 regardless of seasonal variability.

250

251 Figure 6 shows the time series of each carbon tendency component at OSP (within 24 km radius) and in the open ocean (box
 252 in Fig 5c) after removing the linear trend and mean seasonal cycle and applying a 30-day moving window average. First, the
 253 sum of these three tendency components (Eq. 2) exactly matches the DIC tendency (i.e. left-hand side of Eq. 2). The variability
 254 of DIC is almost completely explained by the transport term throughout the entire period, while the effects of the other two
 255 components are relatively minor. At OSP, an extremely negative anomaly in DIC transport convergence rapidly developed in
 256 the winter of 2013, coinciding with the onset of the Blob. This anomaly is unprecedented compared to other periods. In the
 257 open ocean, a negative DIC transport anomaly appeared slightly earlier, in early 2013, and, as at OSP, intensified again in the
 258 winter of 2013. These anomalies led to a pronounced DIC decrease at the onset of the Blob, driven by changes in physical
 259 transport processes.



260

261 **Figure 6:** Time series of vertically integrated DIC tendencies from the surface to 177.5 m at (a) OSP and (b) the open ocean which
 262 is defined in Fig. 5c. The time derivative of DIC is shown in blue; changes in DIC due to transport are shown in orange, due to
 263 biological activity in green, and due to air-sea gas transfer in red. All variables are detrended, deseasonalized, and smoothed using
 264 a 30-day moving average. The unshaded period corresponds to 2014–2015, during which the Blob occurred.

265

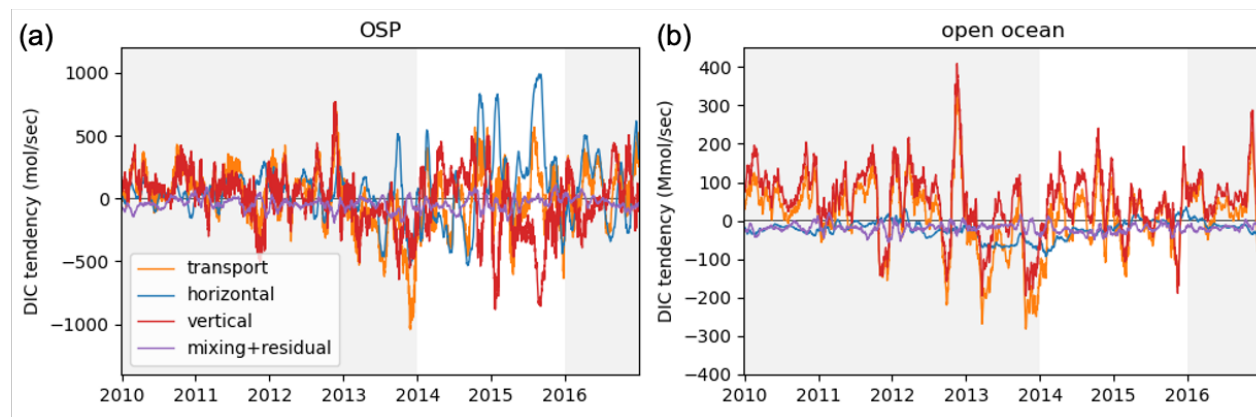
266 To better understand the transport-driven DIC changes, the transport term can be decomposed into individual components
 267 (horizontal and vertical advection) and the parameterized turbulent mixing terms. Among the physical processes responsible
 268 for the DIC reduction during the Blob, the vertical transport dominates over the large-scale domain, whereas locally the effects
 269 of the horizontal transport are comparable to those of the vertical transport. Figure 7 shows the time series of each advective
 270 component of DIC tendency at OSP and in the open ocean. In the open ocean, the transport-driven DIC changes are primarily
 271 controlled by the vertical transport. This is because the small-scale horizontal transport within the computational domain is



272 averaged out, and the transport across the domain boundaries can only play secondary roles in the regional DIC budget.
273 Focusing on the DIC decrease in the winter of 2013, a pronounced reduction associated with the vertical transport is evident,
274 indicating suppressed upward transport of DIC-rich waters from the ocean interior to the surface layer due to enhanced
275 stratification caused by elevated water temperatures. In addition, the decrease in DIC attributable to the horizontal transport is
276 also substantial compared to other years.

277

278 At OSP, the effect of the horizontal transport is more important locally relative to the larger domain in the open ocean. Changes
279 in DIC reflect the combined contributions of the vertical and horizontal transport, and their relative contributions are quantified.
280 In the winter of 2013, the net contribution of the horizontal transport accounted for approximately half of the total DIC decrease
281 ($-531.0 \text{ molCs}^{-1}$), while the remaining half was attributable to a reduction in the vertical transport ($-533.7 \text{ molCs}^{-1}$). This DIC
282 decrease associated with the horizontal transport resulted from strengthened south-easterly currents in the winter of 2013,
283 which advected low-DIC water masses northward, leading to negative DIC anomalies in 2014 (Figs. S1 and S2). Consequently,
284 the local DIC reduction at OSP during the Blob is driven by two mechanisms: anomalous south-to-north transport of low-DIC
285 waters and suppressed upward transport of DIC-rich subsurface waters. These transport anomalies are consistent with the
286 reduced Ekman transport associated with the weakened Aleutian Low that generated the anomalously high sea level pressure
287 and SST (Bond et al., 2015; Hartmann et al., 2015).
288



289

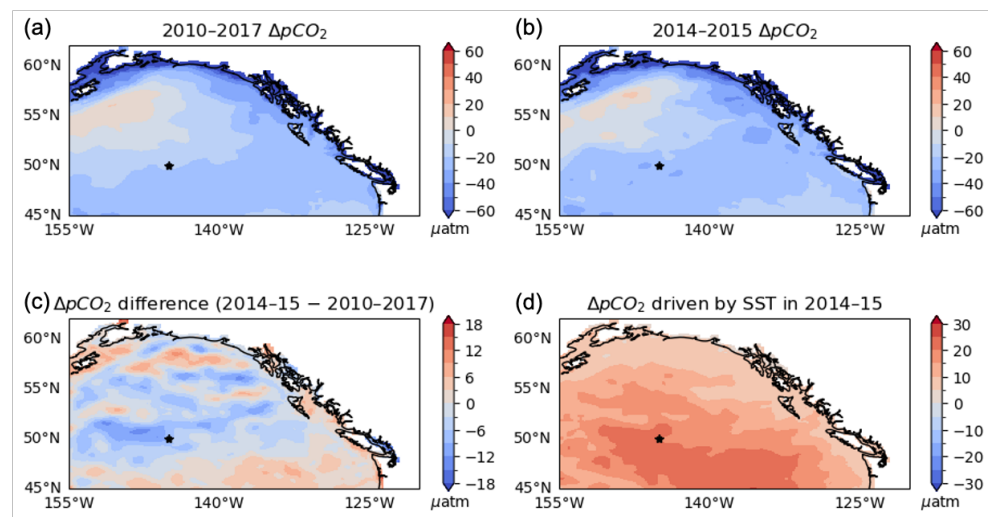
290 **Figure 7: Time series of vertically integrated DIC tendencies from the surface to 177.5 m at (a) OSP and (b) the open ocean, which**
291 **is defined in Fig. 5c, for each transport component: horizontal advection (blue), vertical advection (red), and the mixing and residual**
292 **term (purple), calculated as the remainder after subtracting the advective components from the total transport (orange). All**
293 **variables are detrended, deseasonalized, and smoothed using a 30-day moving average. The unshaded period corresponds to 2014–**
294 **2015, during which the Blob occurred.**

295 4 Discussion

296 Consistent with the observations, the model indicates that increasing SST cannot account for the changes in oceanic pCO_2
297 under the Blob, not only at OSP but across the entire GOA (Fig. 8). Compared to the observations (Fig. 1), ΔpCO_2 driven by



298 SST under the Blob in the model is approximately 5 μatm higher around OSP. Despite the moderate overestimation in thermal-
299 driven pCO_2 anomaly, the modeled ΔpCO_2 shows a significant decrease across the central GOA, consistent with the SeaFlux
300 dataset and the mooring observation at OSP. This consistency is underscoring the robustness of the modeled response.
301 Throughout the region, the effect of warming-induced increase in the oceanic pCO_2 is offset by the oceanic pCO_2 reduction
302 driven by decreased DIC, which is consistent with the previous work by Kohlman et al. (2024).



303
304 **Figure 8: Same as Fig. 1 but for the model results.**

305
306 Our results showed that the reduction in DIC during the Blob was primarily driven by physical processes such as Ekman
307 transport and vertical entrainment. Beyond the oceanic pCO_2 changes, numerous biological impacts of MHWs have also been
308 reported. These include observed declines in annual net community production (Yang et al., 2018), reductions and taxonomic
309 shifts in phytoplankton biomass, transitions in plankton communities from larger to smaller taxa (Du and Peterson, 2018; Peña
310 et al., 2018; Betten et al., 2022). Whether ecosystem impacts can return to pre-MHW conditions remains uncertain (Suryan et
311 al., 2021). The magnitude and nature of these biological responses vary greatly among regions, and a key factor is whether the
312 area is primarily limited by nitrate or iron to the biological production (Peña et al., 2018; Hayashida et al., 2020; Wyatt et al.,
313 2022). Because the GOA is an iron-limited region, it is likely less sensitive to MHW-induced macro-nutrient reductions than
314 regions farther south in the subtropics and the transition zone (30–45°N, Wyatt et al., 2022). Nevertheless, model-based
315 analyses will be essential for assessing long-term and basin-scale impacts. The biogeochemical model used in this study is
316 relatively simple, and it does not explicitly represent shifts in plankton community composition. Revisiting this problem with
317 a more sophisticated ecosystem model would be warranted to assess such ecological changes and determine their duration and
318 magnitude.

319



320 Comparing to the study conducted over broader spatial domains (Mignot et al., 2022), our results reveal a distinct response of
321 oceanic pCO₂ to MHWs in the GOA. This highlights the importance of investigating the impacts of MHWs on oceanic pCO₂
322 in other regions as well. For instance, persistent positive SST anomalies have also been reported in the western North Pacific,
323 particularly in the Oyashio region (40–43°N and 143–147°E, Miyama et al., 2021), which is one of the major carbon uptake
324 areas in the basin. However, it remains unclear how oceanic pCO₂ in this region responded to such anomalies. It is important
325 to expand the model domain to a broader area including the western North Pacific.

326

327 Abnormally high ocean temperatures like the Blob have been increasing both frequency and duration (Frölicher et al., 2018;
328 Oliver et al., 2018). The North Pacific experienced anomalously high SSTs in years such as 2019 (Amaya et al., 2020) and
329 2023 (Dong et al., 2025). These MHWs exhibit even larger SST anomalies than the Blob and differ in several key
330 characteristics, such as the timing of the peak warming (Amaya et al., 2020). Consequently, their impacts on oceanic pCO₂,
331 carbon cycling, and marine ecosystems may differ from those during the Blob. Indeed, the 2023 MHW showed a markedly
332 different behaviour on the global scale, with an approximately 10% reduction in oceanic CO₂ uptake, substantially larger than
333 in previous events (Müller et al., 2025). These contrasts call for event-specific investigations of individual MHWs.

334

335 The model employed in this study was integrated only through 2017 due to the availability of the open boundary conditions.
336 Future work should extend the integration period, for instance by applying alternative boundary conditions, to assess the
337 impacts of the 2019 and 2023 MHWs on oceanic pCO₂.

338 5 Conclusions

339 From the winter of 2013 to 2015, the eastern North Pacific experienced an anomalously high in SST. Contrary to expectations
340 based on the reduced CO₂ solubility under warming, oceanic pCO₂ did not rise. Instead, it decreased across the entire region,
341 with a particularly large decrease in the open ocean (Figs. 1 and 3). To investigate why oceanic pCO₂ broadly decreased during
342 the Blob, the simulation results from the regional ocean circulation and biogeochemistry model were analyzed. The model
343 represents the oceanic pCO₂ remarkably well compared to the observations (Figs. 2 and 3). The decomposition of the oceanic
344 pCO₂ anomalies into four components shows that the variability in the oceanic pCO₂ is primarily dominated by changes in
345 SST and DIC. Furthermore, the effects of these two factors generally compensate for one another. During the Blob, the
346 reduction in oceanic pCO₂ due to a decrease in DIC was stronger in magnitude than the warming-induced increase (Figs. 4 and
347 5). The pronounced reduction in DIC under the Blob is attributable not to biological processes, but rather to the anomalous
348 physical transport (Fig. 6). Typically, DIC-rich water masses are transported from north to south by the wind-driven Ekman
349 transport. However, during the Blob, DIC-poor water masses are advected from south to north (Fig. 7). Furthermore, increased
350 stratification reduced the upward entrainment of subsurface DIC-rich waters. Consequently, these changes in the horizontal
351 and vertical circulation field decreased the surface DIC concentrations, driving a subsequent decline in the oceanic pCO₂.



352

353 **Data availability**

354 The monthly and daily model output data used in this study are archived on Zenodo (doi: 10.5281/zenodo.18462325). The
355 data will be made publicly available upon publication of the associated article.

356 **Author contribution**

357 TI conceptualized and designed the model, and YA performed the simulations and analyses. AT contributed observational
358 comparison and interpretation. YA wrote the original draft of the manuscript. TI, AT, CR, and JM reviewed and edited the
359 manuscript and contributed to scientific discussion. All authors approved the final version of the manuscript.

360 **Competing interests**

361 The authors declare that they have no conflict of interest.

362 **Acknowledgements**

363 This study is supported by the US National Science Foundation (OCE-2241931). The source code for MITgcm is available in
364 the public domain (Campin et al., 2025)

365 **References**

366 Amaya, D. J., Miller, A. J., Xie, S.-P., and Kosaka, Y.: Physical drivers of the summer 2019 North Pacific marine heatwave,
367 *Nat. Commun.*, 11, 1903, doi:10.1038/s41467-41020-15820-w, 2020.

368 Barbeaux, S. J., Holsman, K., and Zador, S.: Marine heatwave stress test of ecosystem-based fisheries management in the Gulf
369 of Alaska Pacific cod fishery, *Front. Mar. Sci.*, 7, 703, doi:10.3389/fmars.2020.00703, 2020.

370 Batten, S. D., Ostle, C., Hélaouët, P., and Walne, A. W.: Responses of Gulf of Alaska Plankton Communities to a Marine Heat
371 Wave, *Deep Sea Research Part II: Topical Studies in Oceanography*, 195, 105002, doi:10.1016/j.dsr2.2021.105002, 2022.

372 Bond, N. A., Cronin, M. F., Freeland, H., and Mantua, N.: Causes and impacts of the 2014 warm anomaly in the NE Pacific,
373 *Geophys. Res. Lett.*, 42, 3414–3420, doi:10.1002/2015gl063306, 2015.

374 Burger, F. A., Terhaar, J., and Frölicher, T. L.: Compound marine heatwaves and ocean acidity extremes, *Nat. Commun.*, 13,
375 4722, doi:10.1038/s41467-022-32120-7, 2022.



376 Campin, J.-M., Heimbach, P., Losch, M., Forget, G., edhill3, Adcroft, A., amolod, Menemenlis, D., dfer22, Jahn, O., Hill, C.,
377 Scott, J., dngoldberg, stephdut, Mazloff, M., Fox-Kemper, B., antnguyen13, Doddridge, E., Fenty, I., Bates, M., Wang, O.,
378 Smith, T., AndrewEichmann, N., mitllheisey, Lauderdale, J., Martin, T., Abernathey, R., samarkhatriwala, hongandyan, and
379 Escobar, I.: MITgcm/MITgcm: checkpoint69e (Version checkpoint69e), Zenodo, doi:10.5281/zenodo.15320163, 2025.

380 Carton, J. A., and Giese, B. S.: A Reanalysis of Ocean Climate Using Simple Ocean Data Assimilation (SODA), *Mon. Weather*
381 *Rev.*, 136, 2999–3017, doi:10.1175/2007MWR1978.1, 2008.

382 Carton, J. A., Chepurin, G. A., and Chen, L.: SODA3: A new ocean climate reanalysis, *J. Clim.*, 31, 6967–6983,
383 doi:10.1175/JCLI-D-17-0149.1, 2018.

384 Cavole, L., Demko, A., Diner, R., Giddings, A., Koester, I., Pagniello, C., Paulsen, M.-L., Ramírez-Valdez, A., Schwenck, S.,
385 Zill, M., and Franks, P.: Biological Impacts of the 2013–2015 Warm-Water Anomaly in the Northeast Pacific: Winners, Losers,
386 and the Future, *Oceanography*, 29, 273–285, doi:10.5670/oceanog.2016.32, 2016.

387 Coyle, K. O., Cheng, W., Hinckley, S. L., Lessard, E. J., Whitledge, T., Hermann, A. J., and Hedstrom, K.: Model and field
388 observations of effects of circulation on the timing and magnitude of nitrate utilization and production on the northern Gulf of
389 Alaska shelf, *Prog. Oceanogr.*, 103, 16–41, doi:10.1016/j.pocean.2012.03.002, 2012.

390 Cronin, M. F., Pelland, N. A., Emerson, S. R., and Crawford, W. R.: Estimating diffusivity from the mixed layer heat and salt
391 balances in the North Pacific, *J. Geophys. Res.-Oceans*, 120, 7346–7362, doi:10.1002/2015jc011010, 2015.

392 Di Lorenzo, E., and Mantua, N.: Multi-year persistence of the 2014/15 North Pacific marine heatwave. *Nature Climate Change*,
393 6 (11), 1042–1047, doi:10.1038/nclimate3082, 2016.

394 Dong, T., Zeng, Z., Pan, M., Wang, D., Chen, Y., Liang, L., Yang, S., Jin, Y., Luo, S., Liang, S., Huang, X., Zhao, D., Ziegler,
395 A. D., Chen, D., Li, L. Z. X., Zhou, T., and Zhang, D.: Record-breaking 2023 marine heatwaves, *Science*, 389, 6758, pp. 369–
396 374, doi: 10.1126/science.adr0910, 2025.

397 Du, X., and Peterson, W. T.: Phytoplankton community structure in 2011–2013 compared to the extratropical warming event
398 of 2014–2015, *Geophys. Res. Lett.*, 45, 1534–1540, doi:10.1002/2017GL076199, 2018.

399 Duke, P. J., Hamme, R. C., Ianson, D., Landschützer, P., Ahmed, M. M. M., Swart, N. C., and Covert, P. A.: Estimating marine
400 carbon uptake in the northeast Pacific using a neural network approach, *Biogeosciences*, 20, 3919–3941, doi:10.5194/bg-20-
401 3919-2023, 2023.

402 Dunne, J. P., Bociu, I., Bronselaer, B., Guo, H., John, J. G., Krasting, J. P., Stock, C. A., Winton, M., and Zadeh, N.: Simple
403 Global Ocean Biogeochemistry with Light, Iron, Nutrients and Gas version 2 (BLINGv2): Model description and simulation
404 characteristics in GFDL's CM4.0, *J. Adv. Model. Earth Sy.*, 12, e2019MS002008, doi:10.1029/2019MS002008, 2020.

405 Emerson, S., Sabine, C., Cronin, M. F., Feely, R., Cullison Gray, S. E., and DeGrandpre, M.: Quantifying the flux of CaCO₃
406 and organic carbon from the surface ocean using in situ measurements of O₂, N₂, pCO₂, and pH, *Global Biogeochem. Cy.*,
407 25, GB3008, doi:10.1029/2010GB003924, 2011.

408 Fay, A. R., Gregor, L., Landschützer, P., McKinley, G. A., Gruber, N., Gehlen, M., Iida, Y., Laruelle, G. G., Rödenbeck, C.,
409 Roobaert, A., and Zeng, J.: SeaFlux: harmonization of air-sea CO₂ fluxes from surface pCO₂ data products using a
410 standardized approach, *Earth Syst. Sci. Data*, 13, 4693–4710, doi:10.5194/essd-13-4693-2021, 2021.



411 Frölicher, T. L., Fischer, E. M., and Gruber, N.: Marine heatwaves under global warming, *Nature*, 560, 360–364,
412 doi:10.1038/s41586-018-0383-9, 2018.

413 Gruber, N., Boyd, P. W., Frölicher, T. L., and Vogt, M.: Biogeochemical extremes and compound events in the ocean, *Nature*,
414 600, 395–407, doi:10.1038/s41586-021-03981-7, 2021.

415 Hartmann, D. L.: Pacific sea surface temperature and the winter of 2014, *Geophys. Res. Lett.*, 42, 1894–1902,
416 doi:10.1002/2015GL063083, 2015.

417 Hauri, C., Schultz, C., Hedstrom, K., Danielson, S., Irving, B., Doney, S. C., Dussin, R., Curchitser, E. N., Hill, D. F., and
418 Stock, C. A.: A regional hindcast model simulating ecosystem dynamics, inorganic carbon chemistry, and ocean acidification
419 in the Gulf of Alaska, *Biogeosciences*, 17, 3837–3857, doi:10.5194/bg-17-3837-2020, 2020.

420 Hayashida, H., Matear, R. J., and Strutton, P. G.: Background nutrient concentration determines phytoplankton bloom response
421 to marine heatwaves, *Global Change Biol.*, 26, 4800–4811, doi:10.1111/gcb.15255, 2020.

422 Hinckley, S., Coyle, K. O., Gibson, G., Hermann, A. J., and Dobbins, E. L.: A biophysical NPZ model with iron for the Gulf
423 of Alaska: reproducing the differences between an oceanic HNLC ecosystem and a classical northern temperate shelf
424 ecosystem, *Deep-Sea Res. Pt. II*, 56, 2520–2536, doi:10.1016/j.dsr2.2009.03.003, 2009.

425 Hobday, A. J., Alexander, L. V., Perkins, S. E., Smale, D. A., Straub, S. C., Oliver, E. C., BenthuySEN, J. A., Burrows, M. T.,
426 Donat, M. G., Feng, M., Holbrook, N. J., Moore, P. J., Scannell, H. A., Sen Gupta, A., and Wernberg, T.: A hierarchical
427 approach to defining marine heatwaves, *Prog. Oceanogr.*, 141, 227–238, doi:10.1016/j.pocean.2015.12.014, 2016.

428 Humphreys, M. P., Lewis, E. R., Sharp, J. D., and Pierrot, D.: PyCO2SYS v1.8: marine carbonate system calculations in
429 Python, *Geosci. Model Dev.*, 15, 15–43, doi:10.5194/gmd-15-15-2022, 2022.

430 Ito, T., Timmerman, H. V. A., Bjorklund, A., Stanley, S. I., Abe, Y., Reinhard, C. T., and Montoya, J.: Eddy-induced iron
431 transport sustains the biological productivity in the Gulf of Alaska. ESS Open Archive.,
432 doi:10.22541/essoar.175080521.18150857/v1, June 24, 2025.

433 Keeling, C. D., Piper, S. C., Bacastow, R. B., Wahlen, M., Whorf, T. P., Heimann, M., and Meijer, H. A.: Exchanges of
434 Atmospheric CO₂ and 13CO₂ with the Terrestrial Biosphere and Oceans from 1978 to 2000. I. Global Aspects, SIO
435 REFERENCE, p. 29, <https://escholarship.org/uc/item/09v319r9> (last access: 06 Oct 2025), 2001.

436 Keeling, C. D., Brix, H., and Gruber, N.: Seasonal and long-term dynamics of the upper ocean carbon cycle at Station ALOHA
437 near Hawaii, *Global Biogeochem. Cy.*, 18, GB4006, doi:10.1029/2004GB002227, 2004.

438 Kohlman, C., Cronin, M. F., Dziak, R., Mellinger, D. K., Sutton, A., Galbraith, M., Robert, M., Thomson, J., Zhang, D., and
439 Thompson, L.: The 2019 marine heatwave at ocean station papa: A multi-disciplinary assessment of ocean conditions and
440 impacts on marine ecosystems, *J. Geophys. Res.-Oceans*, 129(6), e2023JC020167, doi:10.1029/2023JC020167, 2024.

441 Large, W. G., McWilliams, J. C., and Doney, S. C.: Ocean vertical mixing: a review and a model with a nonlocal boundary
442 layer parameterization, *Rev. Geophys.*, 32, 363–403, doi:10.1029/94RG01872, 1994.

443 Lauvset, S. K., Lange, N., Tanhua, T., Bittig, H. C., Olsen, A., Kozyr, A., Alin, S., Álvarez, M., Azetsu-Scott, K., Barbero, L.,
444 Becker, S., Brown, P. J., Carter, B. R., da Cunha, L. C., Feely, R. A., Hoppema, M., Humphreys, M. P., Ishii, M., Jeansson, E.,
445 Jiang, L.-Q., Jones, S. D., Lo Monaco, C., Murata, A., Müller, J. D., Pérez, F. F., Pfeil, B., Schirnick, C., Steinfeldt, R.,
446 Suzuki, T., Tilbrook, B., Ulfso, A., Velo, A., Woosley, R. J., and Key, R. M.: GLODAPv2.2022: the latest version of the



447 global interior ocean biogeochemical data product, *Earth Syst. Sci. Data*, 14, 5543–5572, doi:10.5194/essd-14-5543-2022,
448 2022.

449 Li, C., Burger, F. A., Raible, C. C., and Frölicher, T. L.: Observed Regional Impacts of Marine Heatwaves on Sea-Air CO₂
450 Exchange, *Geophys. Res. Lett.*, 51, e2024GL110379, doi:10.1029/2024GL110379, 2024a.

451 Li, C., Huang, J., Liu, X., Ding, L., He, Y., and Xie, Y.: The ocean losing its breath under the heatwaves, *Nat. Commun.*, 15,
452 6840, doi:10.1038/s41467-024-51323-8, 2024b.

453 Losch, M., Menemenlis, D., Campin, J.-M., Heimbach, P., and Hill, C.: On the formulation of sea-ice models. Part 1: Effects
454 of different solver implementations and parameterizations, *Ocean Model.*, 33, 129–144, doi:10.1016/j.ocemod.2009.12.008,
455 2010.

456 Manizza, M., Le Quéré, C., Watson, A. J., and Buitenhuis, E. T.: Bio-optical feedbacks among phytoplankton, upper ocean
457 physics and sea-ice in a global model, *Geophys. Res. Lett.*, 32, L05603, doi:10.1029/2004GL020778, 2005.

458 Marshall, J., Adcroft, A., Hill, C., Perelman, L., and Heisey, C.: A finite-volume, incompressible Navier Stokes model for
459 studies of the ocean on parallel computers, *J. Geophys. Res.-Oceans*, 102, 5753–5766, doi:10.1029/96JC02775, 1997a.

460 Marshall, J., Hill, C., Perelman, L., and Adcroft, A.: Hydrostatic, quasi-hydrostatic, and nonhydrostatic ocean modeling, *J.*
461 *Geophys. Res.-Oceans*, 102, 5733–5752, doi:10.1029/96JC02776, 1997b.

462 McKinley, G. A., Takahashi, T., Buitenhuis, E., Chai, F., Christian, J.R., Doney, S. C., Jiang, M. S., Lindsay, K., Moore, J.
463 K., Le Quéré, C., Lima, I., Murtugudde, R., Shi, L., and Wetzel, P.: North Pacific carbon cycle response to climate variability
464 on seasonal to decadal timescales, *J. Geophys. Res.*, 111, C07S06, doi:10.1029/2005JC003173, 2006.

465 Mignot, A., Schuckmann, K. V., Landschützer, P., Gasparin, F., Gennip, S. V., Perruche, C., Lamouroux, J., and Amm, T.:
466 Decrease in air-sea CO₂ fluxes caused by persistent marine heatwaves, *Nat. Commun.*, 13, 1–9, doi:10.1038/s41467-022-
467 31983-0, 2022.

468 Miyama, T., Minobe, S., and Goto, H.: Marine Heatwave of Sea Surface Temperature of the Oyashio Region in Summer in
469 2010–2016, *Front. Mar. Sci.*, 7:576240, doi:10.3389/fmars.2020.576240, 2021.

470 Mogen, S. C., Lovenduski, N. S., Dallmann, A. R., Gregor, L., Sutton, A. J., Bograd, S. J., Quiros, N. C., Di Lorenzo, E.,
471 Hazen, E. L., Jacox, M. G., Buil, M. P., and Yeager, S.: Ocean Biogeochemical Signatures of the North Pacific Blob, *Geophys.*
472 *Res. Lett.*, 49, e2021GL096938, doi:10.1029/2021GL096938, 2022.

473 Müller, J. D., Gruber, N., Schneuwly, A., Bakker, D. C. E., Gehlen, M., Gregor, L., Hauck, J., Landschützer, P., and McKinley,
474 G. A.: Unexpected decline in the ocean carbon sink under record-high sea surface temperatures in 2023. *Nat. Clim. Chang.* 15,
475 978–985, doi:10.1038/s41558-025-02380-4, 2025.

476 Oliver, E. C. J., Donat, M. G., Burrows, M. T., Moore, P. J., Smale, D. A., Alexander, L. V., Benthuysen, J. A., Feng, M., Sen
477 Gupta, A., Hobday, A. J., Holbrook, N. J., Perkins-Kirkpatrick, S. E., Scannell, H. A., Straub, S. C., and Wernberg, T.: Longer
478 and more frequent marine heatwaves over the past century, *Nat. Commun.*, 9, 1324, doi:10.1038/s41467-018-03732-9, 2018.

479 Peña, M. A., Nemcek, N., and Robert, M.: Phytoplankton responses to the 2014–2016 warming anomaly in the northeast
480 subarctic Pacific Ocean, *Limnol. Oceanogr.*, 64, pp. 515-525, doi:10.1002/lno.11056, 2018.



481 Reagan, J. R., Seidov, D., Wang, Z., Dukhovskoy, D., Boyer, T. P., Locarnini, R. A., Baranova, O. K., Mishonov, A. V.,
482 Garcia, H. E., Bouchard, C., Cross, S. L., and Paver, C. R.: World Ocean Atlas 2023, Volume 2: Salinity, A. Mishonov,
483 Technical Editor, NOAA Atlas NESDIS 90, doi:10.25923/70qt-9574, 2024.

484 Siedlecki, S. A., Pilcher, D. J., Hermann, A. J., Coyle, K., and Mathis, J.: The Importance of Freshwater to Spatial Variability
485 of Aragonite Saturation State in the Gulf of Alaska, *J. Geophys. Res.-Oceans*, 122, 8482–8502, doi:10.1002/2017JC012791,
486 2017.

487 Smale, D. A., Wernberg, T., Oliver, E. C. J., Thomsen, M., Harvey, B. P., Straub, S. C., Burrows, M. T., Alexander, L. V.,
488 BenthuySEN, J. A., Donat, M. G., Feng, M., Hobday, A. J., Holbrook, N. J., Perkins-Kirkpatrick, S. E., Scannell, H. A., Sen
489 Gupta, A., Payne, B. L., and Moore, P. J.: Marine heatwaves threaten global biodiversity and the provision of ecosystem
490 services, *Nat. Clim. Change*, 9, 306–312, doi:10.1038/s41558-019-0412-1, 2019.

491 Stock, C. A., Dunne, J. P., and John, J. G.: Global-scale carbon and energy flows through the marine planktonic food web: An
492 analysis with a coupled physical–biological model, *Prog. Oceanogr.*, 120, 1–28, doi: 10.1016/j.pocean.2013.07.001, 2014.

493 Suryan, R. M., Arimitsu, M. L., Coletti, H. A., Hopcroft, R. R., Lindeberg, M. R., Barbeaux, S. J., Batten, S. D., Burt, W. J.,
494 Bishop, M. A., Bodkin, J. L., Brenner, R., Campbell, R. W., Cushing, D. A., Danielson, S. L., Dorn, M. W., Drummond, B.,
495 Esler, D., Gelatt, T., Hanselman, D. H., Hatch, S. A., Haught, S., Holderied, K., Iken, K., Irons, D. B., Kettle, A. B., Kimmel,
496 D. G., Konar, B., Kuletz, K. J., Laurel, B. J., Maniscalco, J. M., Matkin, C., McKinstry, C. A. E., Monson, D. H., Moran, J.
497 R., Olsen, D., Palsson, W. A., Pegau, W. S., Piatt, J. F., Rogers, L. A., Rojek, N. A., Schaefer, A., Spies, I. B., Straley, J. M.,
498 Strom, S. L., Sweeney, K. L., Szymkowiak, M., Weitzman, B. P., Yasumiishi, E. M., and Zador, S. G.: Ecosystem response
499 persists after a prolonged marine heatwave, *Sci. Rep.*, 11, 6235, doi:10.1038/s41598-021-83818-5, 2021.

500 Takahashi, T., Sutherland, S. C., Wanninkhof, R., Sweeney, C., Feely, R. A., Chipman, D. W., Hales, B., Friederich, G.,
501 Chavez, F., Sabine, C., Watson, A., Bakker, D. C., Schuster, U., Metzl, N., Yoshikawa-Inoue, H., Ishii, M., Midorikawa, T.,
502 Nojiri, Y., Körtzinger, A., Steinhoff, T., Hoppema, M., Olafsson, J., Arnarson, T. S., Tilbrook, B., Johannessen, T., Olsen, A.,
503 Bellerby, R., Wong, C., Delille, B., Bates, N., and de Baar, H. J.: Climatological mean and decadal change in surface ocean
504 pCO₂, and net sea–air CO₂ flux over the global oceans, *Deep-Sea Res. Pt. 2*, 56, 554–577, doi:10.1016/j.dsr2.2008.12.009,
505 2009.

506 Tsujino, H., Urakawa, S., Nakano, H., Small, R. J., Kim, W. M., Yeager, S. G., Danabasoglu, G., Suzuki, T., Bamber, J. L.,
507 Bentsen, M., Böning, C. W., Bozec, A., Chassagnet, E. P., Curchitser, E., Dias, F. B., Durack, P. J., Griffies, S. M., Harada,
508 Y., Ilicak, M., Josey, S. A., Kobayashi, C., Kobayashi, S., Komuro, Y., Large, W. G., Sommer, J. L., Marsland, S. J., Masina,
509 S., Scheinert, M., Tomita, H., Valdivieso, M., and Yamazaki, D.: JRA-55 based surface dataset for driving ocean-sea-ice
510 models (JRA55-do), *Ocean Model.*, 130, 79–139, doi:10.1016/j.ocemod.2018.07.002, 2018.

511 Yang, B., Emerson, S. R., and Peña, M. A.: The effect of the 2013–2016 high temperature anomaly in the subarctic Northeast
512 Pacific (the “Blob”) on net community production, *Biogeosciences*, 15, 6747–6759, doi: 10.5194/bg-15-6747-2018, 2018.

513 Wyatt, A. M., Resplandy, L., and Marchetti, A.: Ecosystem impacts of marine heat waves in the northeast Pacific,
514 *Biogeosciences*, 19, 5689–5705, doi:10.5194/bg-19-5689-2022, 2022.